Editors' Suggestion

Proof-of-principle e^+ source for future colliders

N. Vallis,* P. Craievich, M. Schär, R. Zennaro, B. Auchmann,† H. H. Braun, M. I. Besana, M. Duda, R. Fortunati, H. Garcia-Rodrigues, D. Hauenstein, R. Ischebeck, E. Ismaili, P. Juranić, J. Kosse, A. Magazinik,† F. Marcellini, T. Michlmayr, S. Müller, M. Pedrozzi, R. Rotundo, G. L. Orlandi, M. Seidel,‡ N. Strohmaier, and M. Zykova

Paul Scherrer Institute, Villigen, Switzerland

(Received 1 September 2023; accepted 6 December 2023; published 17 January 2024)

The PSI Positron Production (P^3 or P-cubed) experiment is a e^+ source and capture system with the potential to increase by an order of magnitude the state-of-the-art e^+ yield normalized to the drive linac energy, a highly desirable goal for future colliders. The experiment is framed in the FCC-ee injector study and will be hosted at SwissFEL, located at the Paul Scherrer Institute in Switzerland. This paper presents the P^3 project at an advanced stage, with an emphasis on a capture system featuring a novel e^+ matching device based on high-temperature superconducting solenoids, followed by two large aperture rf cavities surrounded by normal-conducting solenoids. The diagnostics design is also introduced, including monitors of charge, energy spectrum, and bunch-by-bunch longitudinal profile simultaneously for secondary e^+ and e^-. The last chapter of the text overviews the currently ongoing installation at SwissFEL, including the beam transfer line, rf network, radiation protection, and other relevant activities toward the operation with e^+ in the coming years.

DOI: 10.1103/PhysRevAccelBeams.27.013401

I. INTRODUCTION

Positron (e^+) sources for particle accelerators are almost universally based on pair production through the interaction of high energy electron (e^-) beams with high-Z converter targets [1]. Despite the large e^+ yields provided, particle showers involved in e^+ production are associated with an extreme transverse emittance and energy spread, which require a significantly greater damping than those generated in the average e^- gun. For this reason, e^+ linacs normally rely on solenoid focusing throughout most of their extension to increase e^+ transmission up to the damping ring (DR), where e^+ have their emittance cooled [2]. Focusing is particularly critical near the target, where most operational e^+ sources have used multi-Tesla solenoid fields produced by a normal conducting flux concentrator (FC). However, in addition to the long-standing field strength limits of normal conducting magnets, the mechanical implementation of FCs forces to locate the target significantly upstream from the peak field. These limitations, along with other practical aspects discussed in the following paragraphs, have resulted in a generally poor capture rates, and thus a low e^+ yield at the exit of the DR in all ever existing e^+ accelerators [3].

This is a particularly limiting factor for high-luminosity lepton colliders such as SLC [4] (SLAC, USA), where the all time high e^+ yield was recorded, and SuperKEKB (KEK, Japan) [5], host of the current state-of-the-art e^+ source. Table I overviews e^+ production and injection at these facilities, including key parameters for e^+ injection efficiency: the primary e^- energy, the magnetic strength around the target and the linac, and the iris aperture of the rf capture cavities. Notice that the e^+ yield at the DR, defined as the ratio of e^+ accepted at the DR per primary e^-, is arguably low in spite of multi-GeV drive e^- beams and multi-Tesla solenoid focusing.

The SwissFEL facility [6] (PSI, Switzerland) will host the PSI Positron Production (P^3 or P-cubed) experiment, an e^+ source demonstrator with the potential to improve by an order of magnitude state-of-the-art e^+ yield normalized to the drive linac energy. The experiment layout is shown in Fig. 1, featuring an e^+ source based on a 6 GeV electron (e^-) beam and 17.5 mm-thick (or 5 times the radiation length) amorphous Tungsten target, followed by a capture system consisting of a high-field solenoid system and two rf accelerating cavities. The remarkable e^+ capture capabilities of P^3 are enabled to a great extent by the usage of high-temperature superconducting (HTS) solenoid around the target region, as well as a novel standing wave solution

*nicolas.vallis@psi.ch
Also at EPFL, Lausanne, Switzerland.
†Also at CERN, Geneva, Switzerland.
‡Also at EPFL, Lausanne, Switzerland.

TABLE I. e^+ injection performance overview of SuperKEKB and SLC according to [3].

Operation period	SLC 1989–1998	SuperKEKB 2014 -
Primary e^- energy (GeV)	30–33	3.5
Maximum solenoid field at target (T)	5.5	4.4[a]
Average solenoid field along linac (T)	0.5	0.4
Minimum rf cavity aperture (mm)	18	30
e^+ yield in target region[b]	≈30	≈8
Maximum meas. e^+ yield at DR	2.5 [2]	0.63 [7]

[a]Maximum historical value taking into account the contribution from bridge coils [8].
[b]Approximate values derived from [4] and [5].

for the rf cavities that provides a large iris aperture (see Table II). In addition, a variety of beam diagnostics, whose goal is to demonstrate such an e^+ yield upgrade, will detect simultaneously the e^+e^- bunching structure after the rf cavities and measure the bunch charge and energy spectrum of e^+ and e^- streams separately.

The P^3 project is driven by the luminosity requirements of the future supercollider FCC-ee [10,11], and its results will constitute one of the main deliverables of the FCC-ee injector feasibility study [9,12,13]. Although the experiment is designed to reproduce the beam dynamics of the FCC-ee e^+ source [14], the primary e^- beam current parameters were decreased in order to meet the SwissFEL radiation protection limits. Notice in Table II the differences in bunch charge, repetition rate, and the number of bunches per pulse with respect to the FCC-ee baseline.

TABLE II. Main e^+ source parameters of FCC-ee and P^3.

	FCC-ee [9]	P^3
Energy (GeV)	6	
Maximum solenoid field at target (T)	tbd	12.7
Average solenoid field along linac (T)	0.5	0.45
Minimum rf cavity aperture (mm)	60	40
σ_E	0.1%	
σ_t (ps)	3.33	
σ_x, σ_y (mm)	0.5	
σ_{px}, σ_{py} (MeV/c)	0.06	
Target length (mm)	17.5	
Q_{bunch} (nC)	1.7–2.4	0.20
Repetition rate (Hz)	200	1
Bunches per pulse	2	1

This paper provides a comprehensive overview of the P^3 experiment at a highly advanced design stage, the most emphasis being on the technology that will enable our novel capture system and its associated beam dynamics. The design of the experiment diagnostics is also presented, foreseeing measurements of charge, energy spectrum, and bunch-by-bunch time structure of e^+e^- beams with an extremely high transverse emittance and energy spread. The text concludes with a brief summary of the current installation at SwissFEL, covering the dedicated extraction line, rf power source and the radiation protection bunker of the P^3 experiment. According to the preliminary timeline, the currently ongoing works are expected to conclude by the end of 2025, as operation with e^+ is envisaged for 2026.

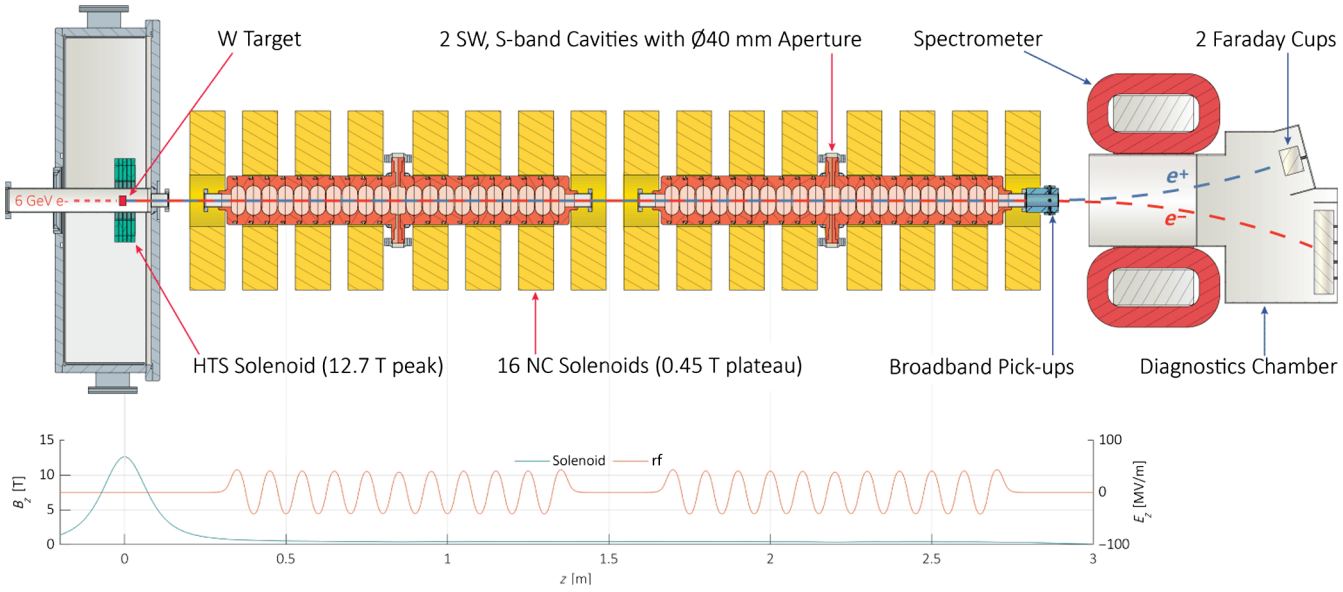

FIG. 1. Simplified layout of the P^3 experiment featuring key components of the e^+ source and capture system (red arrows) and diagnostics (blue arrows). Featuring real dimensions and solenoid and rf field plots at corresponding z.

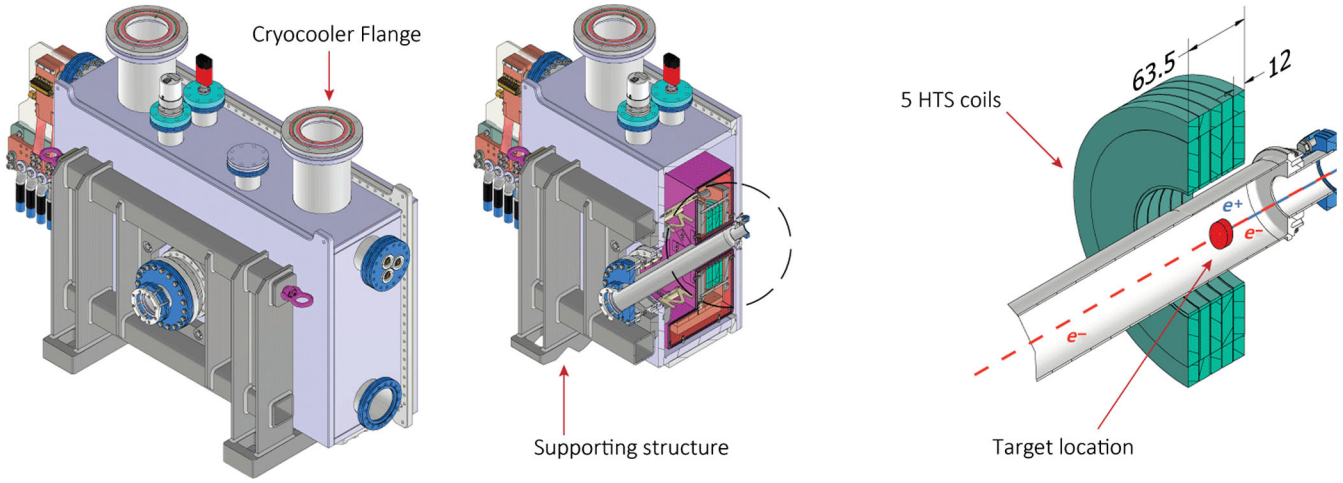

FIG. 2. Assembly of the HTS solenoid, cryostat, and supporting structure (left). Including section view (center) and detail view of the coils and pipe only around the target area (right).

II. KEY TECHNOLOGY

The P^3 experiment will employ novel and conventional technology for e^+ capture and transport from the target to the diagnostics section. As illustrated in Fig. 1, this process will rely on a high-temperature superconducting (HTS) solenoid around the production target followed by 2 rf accelerating cavities surrounded by 16 normal conducting (NC) solenoids.

A. HTS solenoid

Multi-Tesla solenoid fields around the production target are the basis of standard e^+ collection systems [1]. The P^3 experiment will use a high-temperature superconducting (HTS) solenoid in order to deliver a peak 12.7 T on-axis field near the target exit face. As shown in Fig. 2, the HTS solenoid is an arrangement of five coils, which allow for a full immersion of the target in the peak magnetic field. The coils are made out of noninsulated (NI) ReBCO tape, a technology that enables extremely high magnetic strengths, unprecedented in other e^+ sources. This solenoid arrangement increases significantly the e^+ capture capabilities of conventional, normal conducting flux concentrators [15,16]. An analogous HTS solution is considered for FCC-ee, for which P^3 will serve as a demonstrator in most aspects of beam dynamics and operation. However, the lower radiation levels at SwissFEL, with respect to FCC-ee (see Table II), allow for a great simplification of the radiation shielding design. These differences are remarkable in terms of the expected dose per year at the HTS coils (18 kGy in P^3 vs 23 MGy in FCC-ee) and displacements per atom per year ($1e^-8$ DPA vs $2e^-4$ DPA) [17].

NI HTS magnets have demonstrated great stability during high current operation [18,19]. ReBCO tape allows for conduction-cooled, cryogen-free operation at 15 K where the risk of radiation-induced damage to the insulation is negligible [20]. To this end, HTS coils will sit inside a cryostat with two single-stage cryocoolers [21], respectively, dedicated to the coils and the radiation shield and 1.2-kA current leads. Moreover, the conventionally long charging times of NI HTS magnets are significantly reduced due to the compact size of the solenoid. A prototype of the HTS solenoid for P^3, shown in Fig. 3, has been successfully winded, soldered, and stacked in-house. In addition, tests at PSI have demonstrated cryogen-free operation at 15 K and 2 kA, measuring peak magnetic fields of 18 T on axis. The main parameters of the HTS solenoid are collected in Table III.

B. rf cavities

The e^+ capture into stable rf buckets is provided by two S-band, standing wave (SW) cavities shown in Fig. 4, whose parameters are listed in Table IV. A novel SW solution with a large iris aperture of 40 mm diameter will allow for an increased transverse acceptance and while

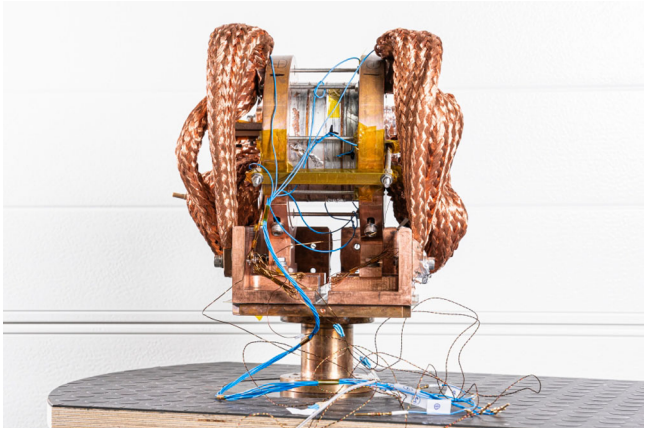

FIG. 3. Prototype assembly of HTS coils with mechanical support and high current leads. Photographed at PSI in June 2022.

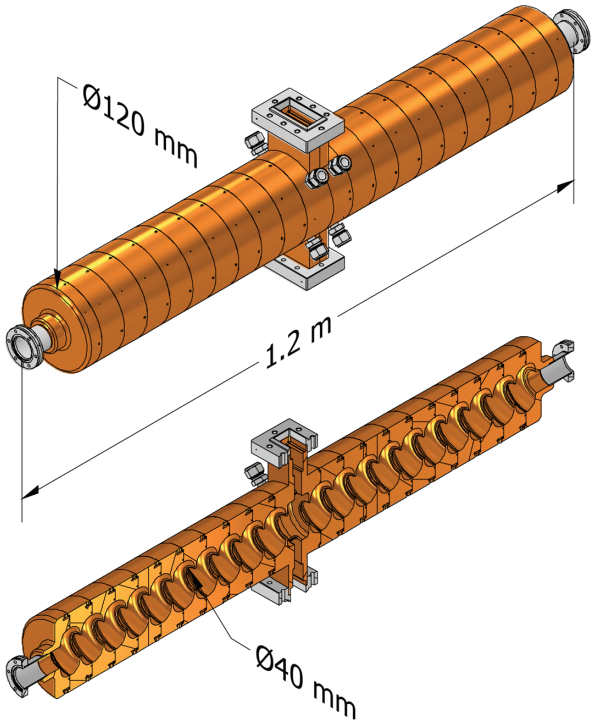

FIG. 4. Mechanical design of rf cavities (top) and section view (bottom).

maintaining a reasonably high shunt impedance. The availability of commercial klystrons and conventional waveguide components in the European S-band determined the frequency choice of 2.9988 GHz. Each cavity is connected to the waveguide network through a double feeder coupler, placed centrally in order to increase the mode separation. One single klystron modulator system, similar to those already installed at the SwissFEL linac, will provide the required peak power and rf pulse length to fill the two cavities and reach a gradient of 18 MV/m. In addition, the coupling factor and the total amount of cells per cavity are optimized for operation with 3 μs rf pulse length. While the normal repetition rates during the experiment will be low (see Table II) the cavities can operate up to 100 Hz, which allows for a reduced conditioning time. The rf phases of both cavities will be adjusted independently through a high-power, in-vacuum phase shifter developed at PSI.

TABLE III. Overview of HTS solenoid parameters.

Conductor	ReBCO tape
Number of coils	5
Thickness (mm)	12
Coil diameter (mm)	122 (inner), 219 (outer)
Aperture (mm)	72
Heat load (W)	9 (at 15 K), 106 (at 40 K)
Maximum magnetic field (T)	15 (on axis), 21 (in conductor)
Operating current (kA)	1.17
Charging time (h)	11

TABLE IV. Overview of rf cavities' parameters.

Length (m)	1.2
rf frequency (GHz)	2.9988 (S-band)
Nominal gradient (MV/m)	18
Number of cells	21
R/L (MΩ/m)	13.9
Aperture (mm)	40
Mode separation (in π mode) (MHz)	5.3
rf pulse length (μs)	3
Coupling factor	2

TABLE V. Overview of normal conducting solenoid parameters.

Length (mm)	112
Coil diameter (mm)	160 (in.), 556 (out.)
Peak field single solenoid (T)	0.213
Current (A)	220
Layers, windings per layer	22, 12
Power consumption per solenoid (kW)	6.5

C. Solenoids around rf cavities

About 16 normal conducting solenoids will surround the rf cavities in a nearly uniform distribution, as illustrated in Fig. 1. Each of which will generate a peak field of 0.22 T, which combined will generate the desired 0.45 T plateau along the beam axis. These solenoids, shown in detail in Fig. 5, are winded into 22 layers and 12 helical windings per layer, with 5 mm diameter channels for water cooling. The solenoid length is 112 mm, and the aperture and outer diameter are 160 and 556 mm, respectively, and no iron yoke is included for maximum field flatness. Feeding with 220 A will be provided separately in two groups of eight solenoids, equivalent to a current density limit of 5 A/mm^2, hence the voltage drop per solenoid is 30 V, which results in a power consumption of 6.5 kW. Cooling can be provided through six channels, with a maximum pressure and water speed of 1 bar and 1 m/s, as well as an inlet-outlet temperature rise of 20 °C. Each solenoid will be encased in an aluminum support, as illustrated in Fig. 5, that will withstand the individual 130 kg copper weight as well as the forces exerted by magnetic interaction with other solenoids. According to simulations, such forces would be as high as 23.5 kN, reaching the peak in the most upstream normal conducting solenoid due to its proximity to the HTS peak field. Notice also in Fig. 2 the large supporting structure around the HTS cryostat. A summary of the normal-conducting solenoids is shown in Table V.

III. BEAM DYNAMICS

The rf and solenoid systems described in Sec. II will drive the beam with unprecedented efficiency from the target up to the diagnostics section. The beam dynamics associated in this process will be elucidated in this chapter, with a particular emphasis on the key factors behind the e^+ yield

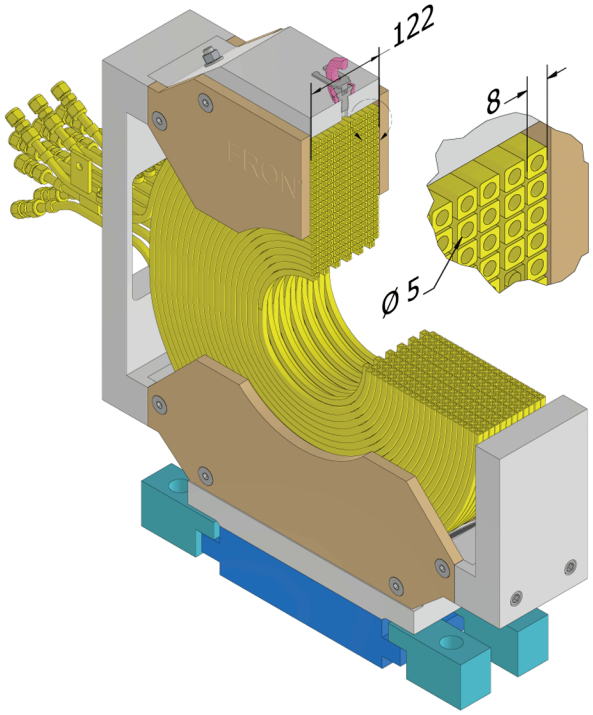

FIG. 5. Mechanical design of solenoids around rf cavities and supporting structure. Including section and detail view of windings and cooling channels.

upgrade: an abundant e^+ production at the target, high solenoid peak fields around the target, a uniform magnetic channel along the rf cavities combined with a large iris aperture and a comprehensive rf phase optimization. Studies are based on Geant4 [22] and ASTRA [23] simulations.

A. e^+ production at target

e^- bunches of 200 pC at 6 GeV will impinge upon the 17.5 mm-thick Tungsten target according to parameters in Table II, yielding an e^+e^- beam in the multi-MeV and nano-Coulomb range. Transverse and longitudinal profiles of the secondary e^+ distribution are shown in Fig. 6, corresponding to beam parameters listed in Table VI.

TABLE VI. Main parameters of charge, and transverse and longitudinal dynamics of the e^+ beam at the target exit and the entrance of the first rf cavity.

	Target exit[a]	First rf cavity entrance[b]
Q_{e^+} (pC)	2754	2334
N_{e^+}/N_{e^+}	13.77	11.67
σ_x, σ_y (mm)	1.1	6.2
σ_{px}, σ_{py} (MeV/c)	7.1	2.7
$\epsilon_{x,\mathrm{norm}}$, $\epsilon_{y,\mathrm{norm}}$ (πmm mrad)	11676	12016
σ_t (ps)	5.7	11.3
ΔE_{rms} (MeV)	122.8	

[a]Simulated with Geant4 according to parameters in Table II.
[b]Simulated with ASTRA on the basis of a.

Longitudinally, secondary bunches emerging from the target will have a length ($\sigma_t = 5.7$ ps) comparable to that of primary e^- ($\sigma_t = 3.3$ ps). However, the secondary uncorrelated energy spread ($\Delta E_{\mathrm{rms}} = 122.8$ MeV) will be significantly greater. Similarly, in the transverse plane, despite the moderate beam size at the target exit ($\sigma_x = 1.1$ mm), e^+ will have a large uncorrelated spread of transverse momentum ($\sigma_{px} = 7.1$ MeV/c). These values indicate that e^+ dynamics are heavily dominated by an extreme transverse emittance and energy spread.

Primary e^- beam parameters, with the exception of beam current, are inherited from previous optimization works for FCC-ee [14], aimed at high e^+ production rates and tolerable energy deposition levels at the target. As a rule, high energies of the e^- drive beam are desirable, as electromagnetic showers developing in the multi-GeV regime will generate greater e^+ yields and a small transverse size of the primary e^- beam also leads to higher acceptance. In addition, there is an optimum target thickness associated with energy [24], which in the FCC-ee case is 17.5 mm. Nevertheless, primary energy and transverse size are limited by the drive linac capabilities, and by thermomechanical factors and intrinsic properties of the

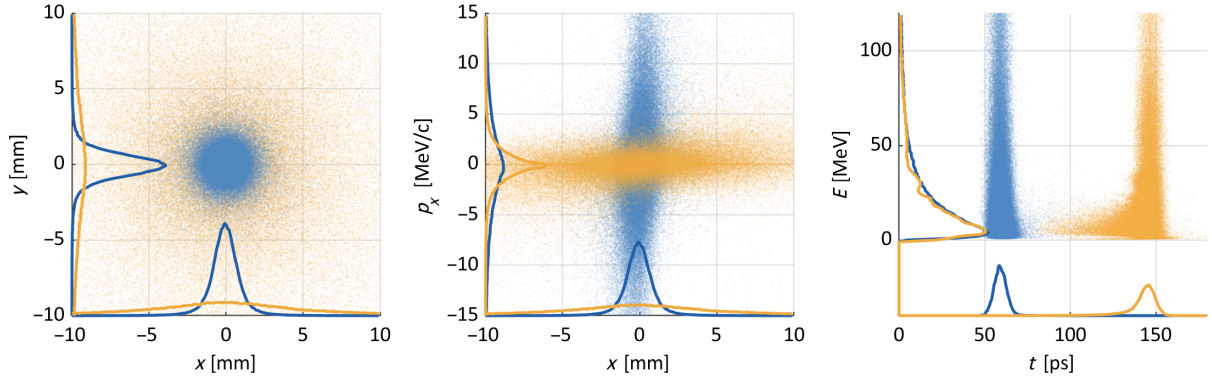

FIG. 6. Transverse and longitudinal profiles of the e^+ distribution at exit face of the target (blue) and at the entrance of first rf cavity (yellow). Corresponding statistical values found in Table VI.

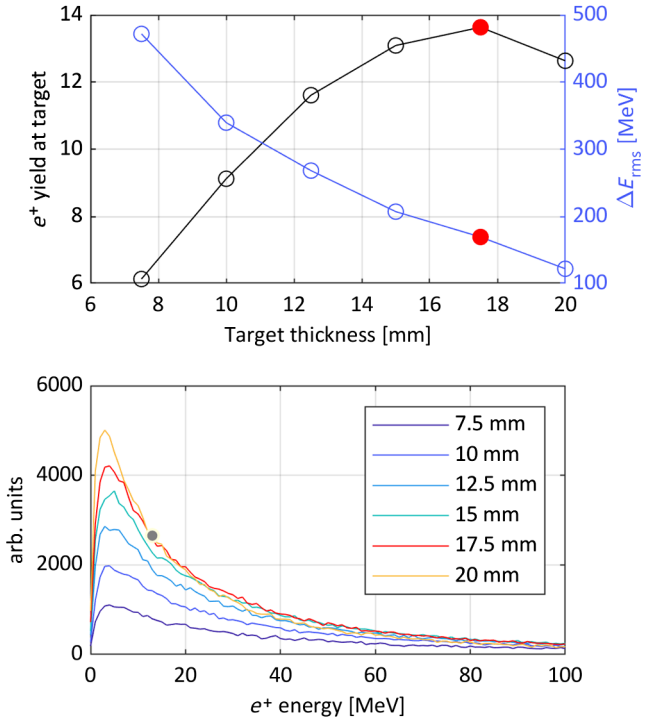

FIG. 7. e^+ yield at the target and rms energy spread with respect to target thickness, assuming 6 GeV primary e^- beam (top). e^+ energy distributions for different target thickness values (bottom). Current baseline, 17.5 mm, shown in red.

target material. A benchmark optimization study was performed for P^3. Figure 7 shows a target thickness scan considering 6 GeV, 0.5 mm primary e^-, where a clear maximum (13.77 N_{e^+}/N_{e^-}) is reached at 17.5 mm, as found in previous studies for FCC-ee. It is also observed that a greater target thickness can reduce the rms energy spread, but the 17.5 mm baseline is maintained in order to keep consistency with the FCC-ee parameters. Note that no thermomechanical studies are presented due to the extremely low e^- drive current foreseen in P^3.

Due to the extreme transverse emittance inherent particle showers, some e^+ may emerge from the target with an extremely high transverse momentum p_x, leading to a divergence (p_x/p_z) well above 1. Despite representing a small portion of the e^+ charge, these particles may significantly inflate the emittance calculations. To avoid these effects, the core emittance [25] is calculated for different beam slices, defined within the equivalent Twiss ellipses. As shown in Fig. 8, particles encompassed by the nominal Twiss ellipse (1σ) have an emittance of 7486 π mm mrad. The 3σ ellipse, which comprises 95% of e^+ at the target exit, yields an emittance of 11676 π mm mrad. In this framework, there is little margin for emittance reduction, since the secondary p_x spread is fairly insensitive to primary e^- energy and size. However, further e^+ yield maximization and emittance cooling through alternative target geometries are currently under study and will be tested during the P^3 experiment.

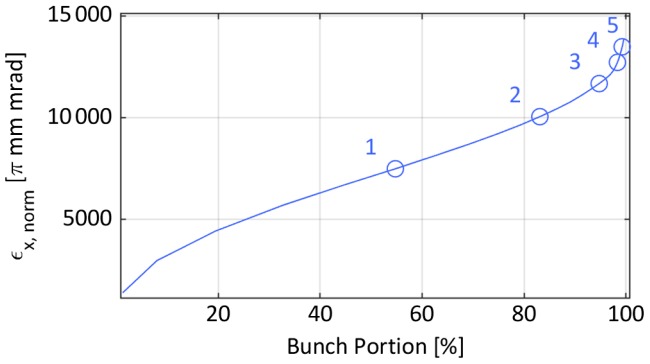

FIG. 8. Normalized transverse core e^+ emittance [25] at the target exit for different beam slices, defined as Twiss ellipse fittings. Numbers next to data points represent σ, or the semiaxes sizes, 1σ being the nominal Twiss parameters.

B. Transverse e^+ capture through high solenoid fields

Like most preceding e^+ linac designs [3], P^3 relies on a solenoid system for e^+ collection. The solenoid arrangement and associated field profile shown in Fig. 1 make up an adiabatic matching device (AMD) [26,27], a well-known e^+ capture technique based on an adiabatic transformation of the transverse phase space of newly generated e^+ (moderate σ_x and large σ_{px}) to better fit the acceptance of the capture system (large σ_x and moderate σ_{px}). The adiabatic approach is adopted under the assumption that particles will describe many spiraling trajectories along the solenoid channel, and thus rotation frequency will slowly diminish as the high peak solenoid field around the target (12.7 T) decreases toward the magnetic plateau around the capture line (0.45 T). The action integral $\int_0^\tau E_\perp dt$ will therefore be an adiabatic invariant [28]. The effect of the AMD is clearly illustrated in Fig. 6 and listed in Table VI, where compression of the transverse momentum spread ($\sigma_{px} = 2.7$ MeV/c) is compensated by a beam size growth ($\sigma_x = 6.2$ mm) well below the aperture of the rf cavities (40 mm diameter).

The 0.45 T plateau delivered by the NC solenoids will create a magnetic channel along the rf cavities with the ability to capture and transport a large proportion of the matched e^+. This magnetic profile is fairly uniform, as shown in Fig. 9, besides relatively small drops around $z = 0.86$ m and $z = 2.21$ m, where the separation between solenoids is slightly incremented in order to fit the waveguide couplers of the rf cavities. According to Fig. 10, the proposed solenoid arrangement would provide capture efficiencies as high as 45.7% with the ability to transport transverse normalized emittances around 4000 π mm mrad. Greater transmission rates are reachable through the use of multi-Tesla magnetic channels generated by low temperature superconducting solenoids, as considered in previous design versions [29]. However, 0.45 T fields show a good performance while avoiding excessive costs and power consumption.

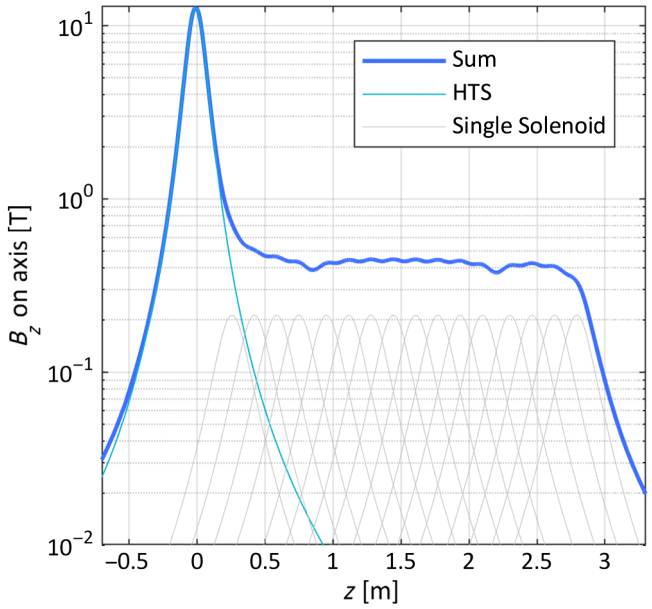

FIG. 9. Detail view of solenoid field profile on axis along the capture section. Including contributions of HTS and normal conducting solenoids.

C. rf bunching and acceleration

Secondary e^+e^- will emerge from the target under the influence of the 12.7 T solenoid field, describing spiraling trajectories with a wide range of Larmor angles and *radii* due to their extremely large energy spread [1]. This effect will make newly generated particle distributions grow longitudinally ($\sigma_t = 11.3$ ps), as illustrated in Fig. 6 and Table VI. As a result, rf fields will generate time structures of many consecutive e^+ and e^- bunches separated by $\lambda/2$ (167 ps or 50 mm in the ultrarelativistic regime). Although different rf configurations lead to diverse bunching profiles, in most cases, a great proportion of particles are captured over the first two rf buckets. The typical bunching profile of P[3] is well described in Fig. 12.

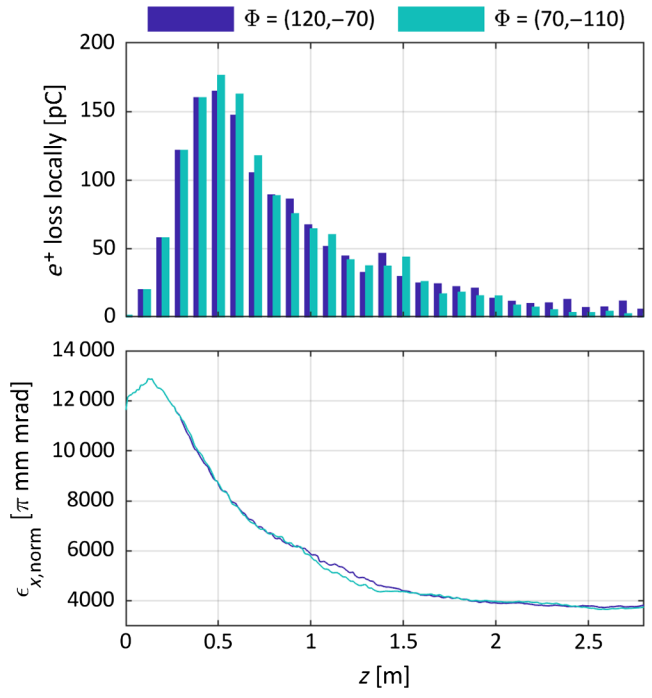

FIG. 10. Simulated local e^+ charge loss (top) and normalized transverse emittance (bottom) along the rf cavities. Calculated for rf working points of interest calculated in Sec. III C.

Regarding the rf optimization, two main figures of merit (FOMs) are considered: the total captured e^+ charge at the exit of the second rf cavity and the equivalent e^+ yield at the FCC-ee DR (see Sec. I). While the first FOM corresponds to a real, measurable quantity, the latter will establish a correction factor with respect to the equivalent charge accepted at the FCC-ee DR. Such yield is computed through e^+ tracking up to 200 MeV, extending the baseline simulation layout from two to ten rf cavities surrounded by solenoids. The resulting longitudinal time-energy distribution at 200 MeV is transformed analytically up to 1.54 GeV, the nominal energy of the FCC-ee DR, where a filter in energy of $\pm 3.8\%$ is applied. Notice that this analytical approach is proven highly accurate with respect to 6D particle tracking simulations, due to the small transverse losses above 200 MeV and the absence of radial dependency of the accelerating electric field within the iris area [16].

Both figures of merit, as represented in Fig. 11, are strongly dependent on the rf phase setting. Among all possible configurations, two working points of interest (see Table VII) were chosen: $\Phi = (120, -70)$, which provides maximum e^+ capture of 1246 pC after the second rf cavity, and $\Phi = (70, -110)$, corresponding to the maximum e^+ yield of 4.64 N_{e^+}/N_{e^-} at the FCC-ee DR. Notice that due to the large beam spread, it is difficult to establish a definition of bunch center. For this reason, the rf phases introduced throughout this paper are arbitrary, with notions such as rf crest or zero crossing having no particular physical meaning.

Major differences between the rf working points of interest are observed at the exit of the second rf cavity. Figure 12(a), corresponding to $\Phi = (120, -70)$, shows an extremely spread and smooth energy profile ranging from below 20 to above 50 MeV. Longitudinally, e^+ is concentrated toward the high-energy tail downstream from the main rf bucket. Instead, the $\Phi = (70, -110)$ case illustrated in Fig. 12(b) shows a greater e^+ population around the crest of the main rf bucket. In addition, despite also showing a large energy spread, particle concentration is more clearly observed around 20 MeV. Such differences are even more noticeable at the DR energy of 1.54 GeV, provided by the excellent bunching at $\Phi = (70, -110)$, as shown in Fig. 13(b). It contrasts with the largely spread energy profile in Fig. 13(a), which leads to a lower yield at the

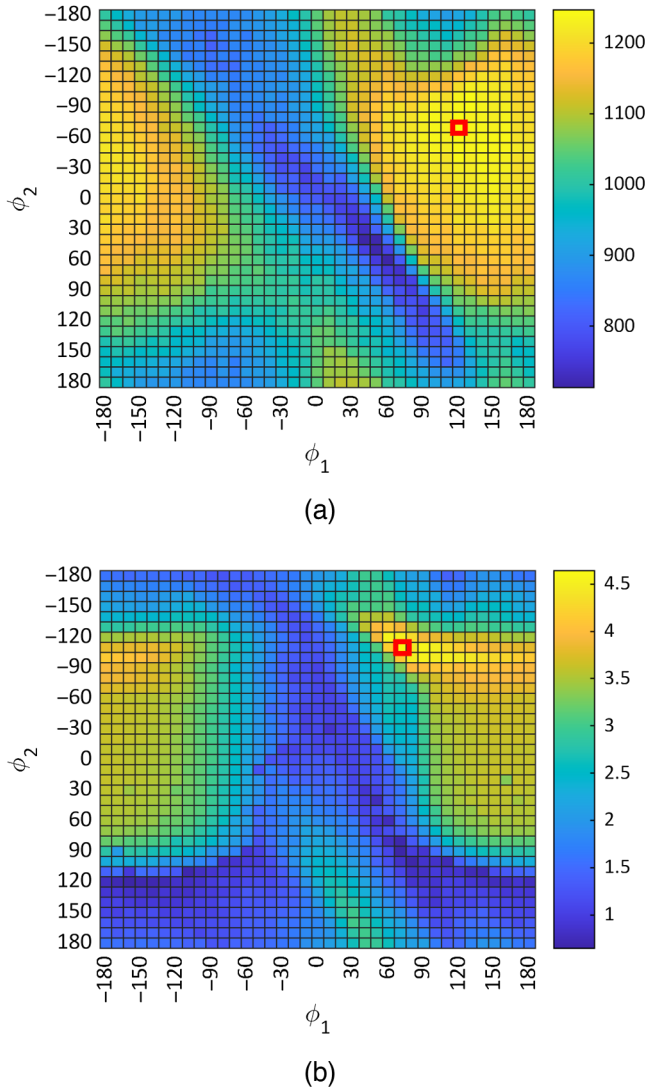

FIG. 11. Total e^+ captured charge in pC (a) and estimated e^+ yield at the FCC-ee DR (b) simulated over full 2D rf phase scan. $\Phi = (120, -70)$ and $\Phi = (70, -110)$ marked in red in (a) and (b), respectively.

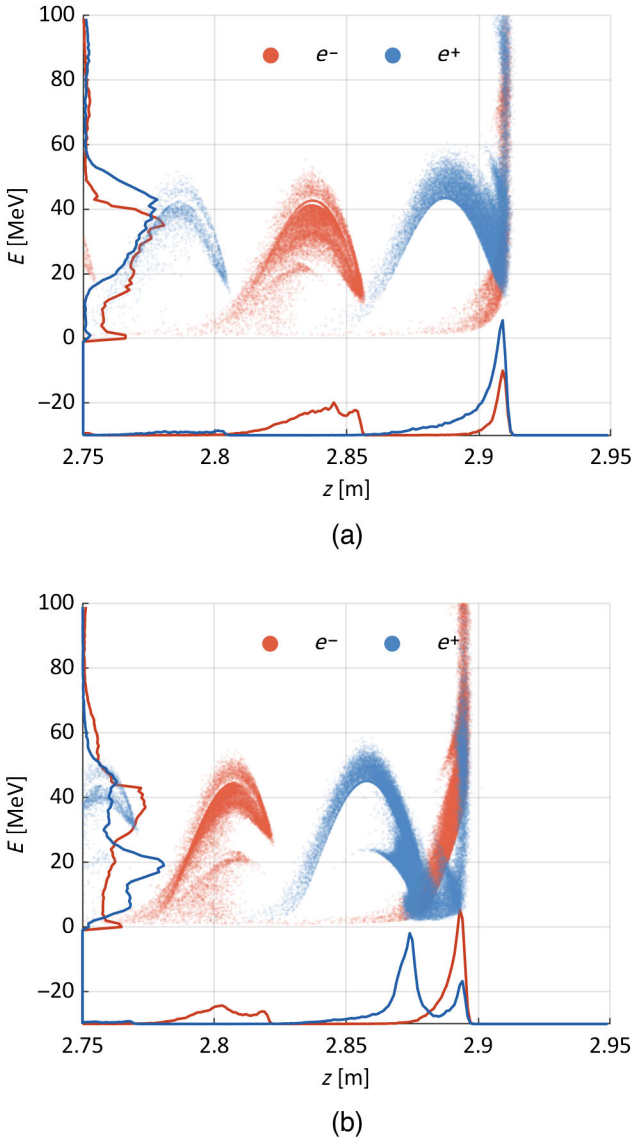

FIG. 12. Simulated e^+e^- distributions near the exit of the second rf cavity ($z \approx 2.8$ m) for rf working points of interest: $\Phi = (120, -70)$ (a) and $\Phi = (70, -110)$ (b). Notice that longitudinal dimension is given in units of length.

FCC-ee DR despite having the highest e^+ charge capture rates.

Figure 14 gives a particularly good explanation of the energy compression process, showing how particles at 1, 5, and 12 MeV reach almost the same energy at the exit of the second rf cavity, achieved through a partial deceleration of the beam in the $\Phi = (70, -110)$ case. Interestingly, the use of decelerating rf modes is an energy compression technique well suited for e^+ sources [30]. Notice that the $\pm 3.8\%$ energy acceptance filter of the DR may be subject to future changes. Therefore, we provide in Fig. 15 a scaling factor for different energies applied to both rf working points of interest for a range of DR acceptance parameters.

TABLE VII. e^+ charge and yield provided by rf working points of interest.

	Second rf cavity exit	FCC-ee DR
$\Phi = (120, -70)$	1246 pC 6.23 N_{e^+}/N_{e^-}	768 pC 3.84 N_{e^+}/N_{e^-}
$\Phi = (70, -110)$	1153 pC 5.77 N_{e^+}/N_{e^-}	928 pC 4.64 N_{e^+}/N_{e^-}

IV. BEAM DIAGNOSTICS

The P^3 diagnostics section is illustrated in Fig. 16, equipped with an arrangement of broadband pickups (BBPs), two Faraday Cups (FCs), and a variety of scintillating detectors, including screens and fibers. The BBPs

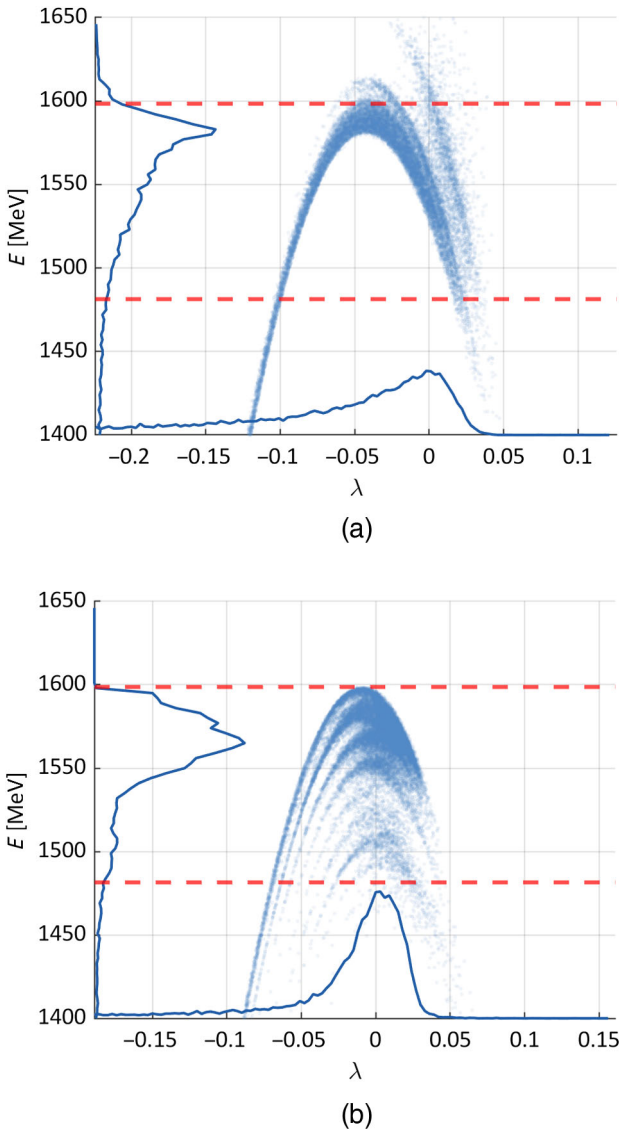

FIG. 13. Estimated e^+ distributions at entrance of the FCC-ee DR for rf working points of interest: $\Phi = (120, -70)$ (a) and $\Phi = (70, -110)$ (b). Red dashed lines represent energy acceptance of DR, $\pm 3.8\%$ of 1.54 GeV. Notice that longitudinal dimension is given in terms of wavelength (λ), zero corresponding to the rf crest.

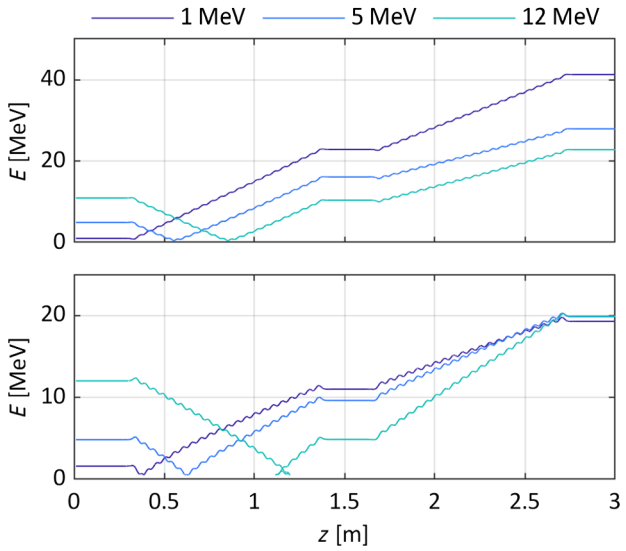

FIG. 14. Simulation of e^+ at different initial energies accelerated by the P^3 rf cavities, for rf working points of interest: $\Phi = (120, -70)$ (top) and $\Phi = (70, -110)$ (bottom).

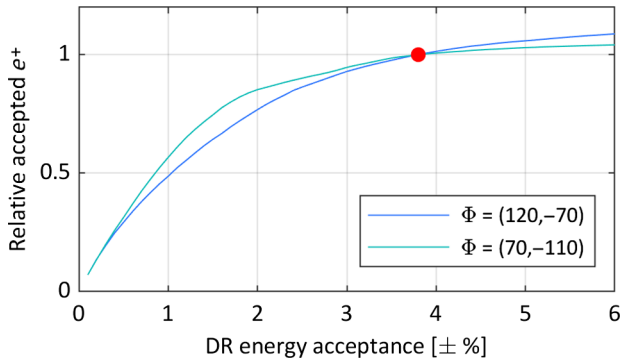

FIG. 15. Relative yield at the DR with respect to the energy acceptance. Current baseline of $\pm 3.8\%$ is marked in red.

will detect the time structure of the captured e^+e^- beam. The FCs and scintillators will be installed in the same vacuum chamber and will measure the charge and energy spectrum of e^+ and e^- streams independently. Separation of particle species will be provided by a spectrometer, a dipole magnet based on four copper coils, and an iron yoke, which will be fed at a maximum current of 340 A in order to reach magnetic fields up to 0.25 T.

A. Broadband pickups

An arrangement of four broadband pickups (BBPs), shown in Fig. 17, will follow the exit of the second rf cavity. The BBPs will detect simultaneously the image charges generated by the e^+ and e^- bunches and reconstruct their time structure, including bunch-by-bunch measurements of charge, length, and separation. The e^+e^- time structure will depend on the rf phase configuration, yet the typical distribution (see Fig. 12) will consist of alternating e^+ and e^- bunches of 33 ps length and separated by 167 ps, namely half S-band period. Measurements in the picosecond range require a broad frequency response, thus the geometry of the pickups is optimized to avoid intrinsic resonances up to frequencies in the range of a few tens of GHz while providing a relatively high peak voltage. According to a preliminary simulation based on a Gaussian approximation of the P^3 bunches, the BBPs would detect a ± 4.5 V peak voltage signal with very small distortion, as seen in Fig. 18. Notice that this simulation does not take into account cable distortion or noise.

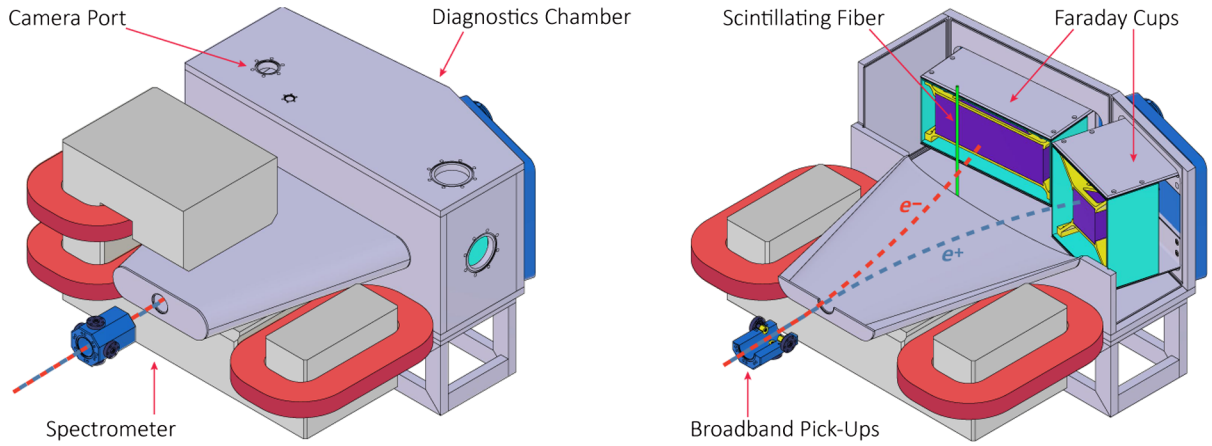

FIG. 16. P^3 diagnostics setup (left) including inside view (right).

Two BBP assemblies have been developed and fabricated, based on broadband vacuum feedthroughs up to 27 GHz [32] (shown in Fig. 17) and 65 GHz [33]. The hardware acquisition setup will consist of low attenuation, broadband cables [34], and a high-end oscilloscope of at least 10 GHz passband and sampling rates around 100 GS/s. Both BBP assemblies will be tested in different e^- facilities before installation in P^3 in order to study major potential issues not covered by simulations, such as wakefield effects. Similar solutions based on ultrafast pickups are currently in use, such as the fast BPMs at the SuperKEKB e^+ linac [35,36] and the bunch arrival time monitors at SwissFEL [37].

B. Faraday cups

As illustrated in Fig. 16, the spectrometer will deflect the e^+ and e^- streams into opposite directions, ending in a highly asymmetrical arrangement of Faraday cups (FCs). Despite the extremely high dispersion introduced by the spectrometer due to energy (and p_z) spread, both FCs are designed to collect a great proportion of the e^+ and e^-. Each FC will achieve particle collection through áan entirely different principle. However, both of them would provide similar charge measurements for both species, which could be delivered to either FC through a sign inversion of the spectrometer polarity.

The first FC is tuned at 12.5 Ω in pursuit of a large transverse area (260 × 90 mm), which will maximize the collection of charged particles in a wide energy range of 9–75 MeV. The coaxial impedance, a factor of 4 smaller than the 50 Ω standard, allows to reduce the size of the outer conductor and can be easily matched to standard circuits through the use of four parallel coaxial cables in the output, which will be read independently. A second, relatively compact FC (80 × 80 mm) tuned at 50 Ω will detect charged particles in a larger energy range of 3–90 MeV. Although this transverse size does not allow for single-shot charge measurements in broad energy spectra, the 50 Ω FC will allow for energy discriminating measurements by adjusting the spectrometer strength, which determines the energy range of the particles routed toward the FC. A scan of six magnetic field values, indicated in

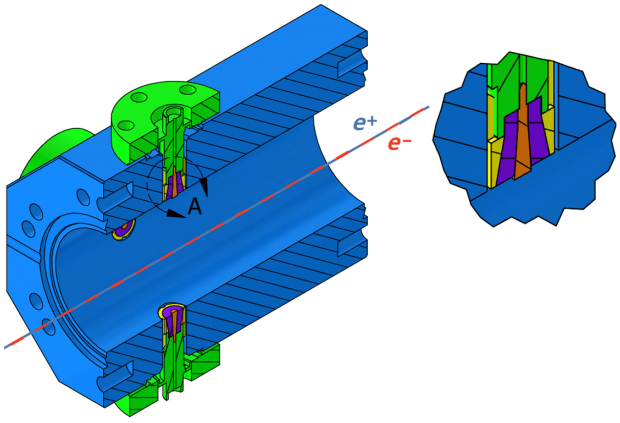

FIG. 17. Mechanical design of the 27 GHz BBP assembly. Detail view A features a pickup (orange) with its corresponding dielectric PTFE holder (purple) and outer conductor (yellow) mounted on a feedthrough (green).

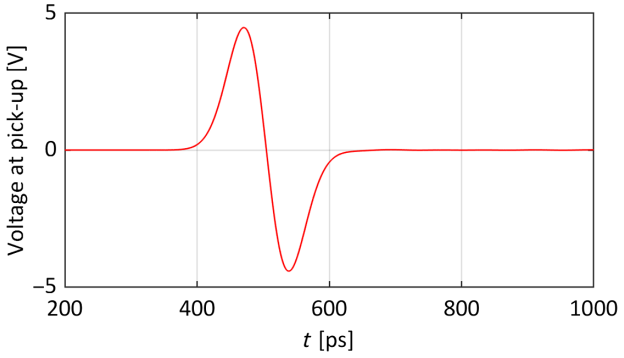

FIG. 18. Detected voltage signal by one pickup using 27 GHz feedthrough arrangement. Signal generated by Gaussian bunch of $Q_{bunch} = 1$ nC and $\sigma_t = 33$ ps. Simulated with CST [31].

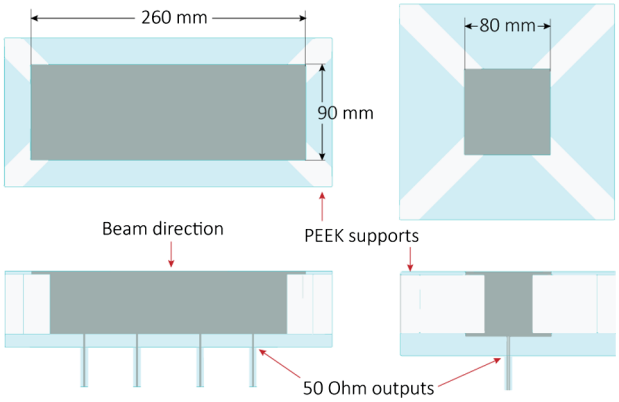

FIG. 19. Electromagnetic design of 12.5 Ω (left) and 50 Ω (right) FCs, including tungsten blocks, PEEK supports, and vacuum space.

Table VIII, would cover the above mentioned 3–90 MeV range. Figure 20 shows the frequency response of both FC arrangements with four diagonal PEEK supports (as seen in Fig. 19), in both cases above 1 GHz.

Error estimations of the measured e^+ charge are shown in Fig. 21 for both FC layouts and all rf phase configurations, showing a reasonably good agreement with Fig. 11, particularly in the vicinity of the rf working point of interest. These error studies are based on ASTRA particle tracking simulations. At $\Phi = (120, -70)$, the point where maximum e^+ capture is achieved, the 12.5 and 50 Ω FCs would read −13.6% and −9.4% with respect to the expected 1246 pC. This rf working point was studied in

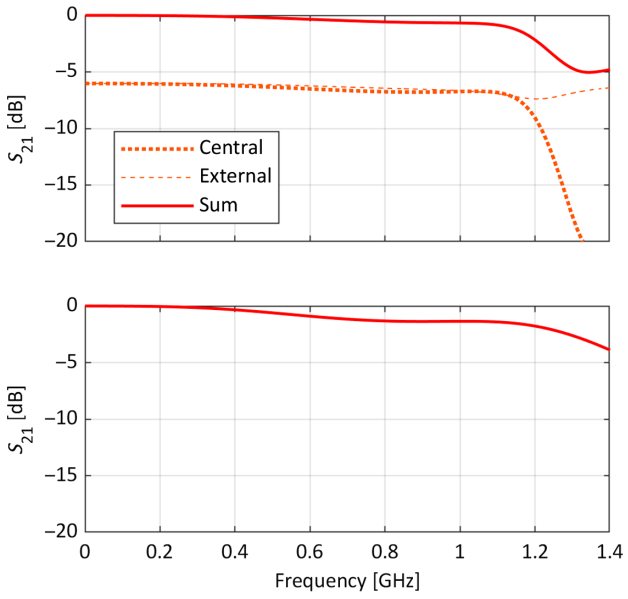

FIG. 20. Transmission losses of 12.5 Ω (top) and 50 Ω (bottom) FCs. In the 12.5 Ω case, individual output response included for innermost and outermost connectors. Based on HFSS [38] simulations including tungsten blocks, PEEK supports, and vacuum space, according to layouts illustrated in Fig. 19.

TABLE VIII. Reference spectrometer strength and measured energy ranges for different channels of FCs. Values based on zero-emittance particles.

	Spectrometer strength (T)	Measured energy range (MeV)
12.5 Ω FC	0.053	9–75
50 Ω FC	0.212	50–90
	0.120	28–50
	0.068	16–28
	0.038	9–16
	0.021	5–9
	0.012	3–5

further detail with GEANT4 simulations. 60 mm-thick W blocks were considered for both FCs in order to maximize charge deposition. Notice that as for now, backscattering effects due to the high tungsten density are disregarded as they are small in the multi-MeV range and negligible above 10 MeV. The results obtained indicate a deposited e^+ charge of 1058 pC in the 12.5 Ω FC and 1164 pC in the 50 Ω one, namely −15.0% and −6.6% with respect to 1246 pC. On the other hand, poorer charge measurements are expected at lower energies, as particle divergence will have a greater impact on the final transverse position. For this reason, e^+ charge can be underestimated by as much as −58% and −33% by the 12.5 and 50 Ω FCs, respectively. However, this occurs in regions with relatively small importance for the experiment.

C. Scintillators in diagnostics chamber

The diagnostics chamber hosting the FCs will accommodate at least two additional setups based on scintillator materials. First, the front face of the FCs will have scintillating screens that will allow cameras mounted outside of the chamber to look at the collected e^+ and e^- distributions. Besides being particularly useful during beam commissioning, the screens will provide a spectral measurement of the energy profiles. However, the large size of the FCs and the transverse emittance of the beam result in a very poor energy resolution. The scintillator can either be a coating deposited on the face of the FCs, a screen mounted to the front of the FCs, or a free-standing screen that can be inserted in and out of the chamber. The most likely materials for the screen would be Cr-doped alumina (Chromox), Biomax, or YAG, which have been used for scintillation in accelerators in the past [39].

An alternate high-resolution spectroscopic setup consisting of at least one pair of scintillator fibers will reconstruct the longitudinal momentum (p_z) spectrum of the e^+ and e^- distributions. The fibers, vertically oriented, will be hit by a small fraction of the particles corresponding to a narrow division of the energy spectrum, allowing to scan the p_z spectrum by changing the dipole strength

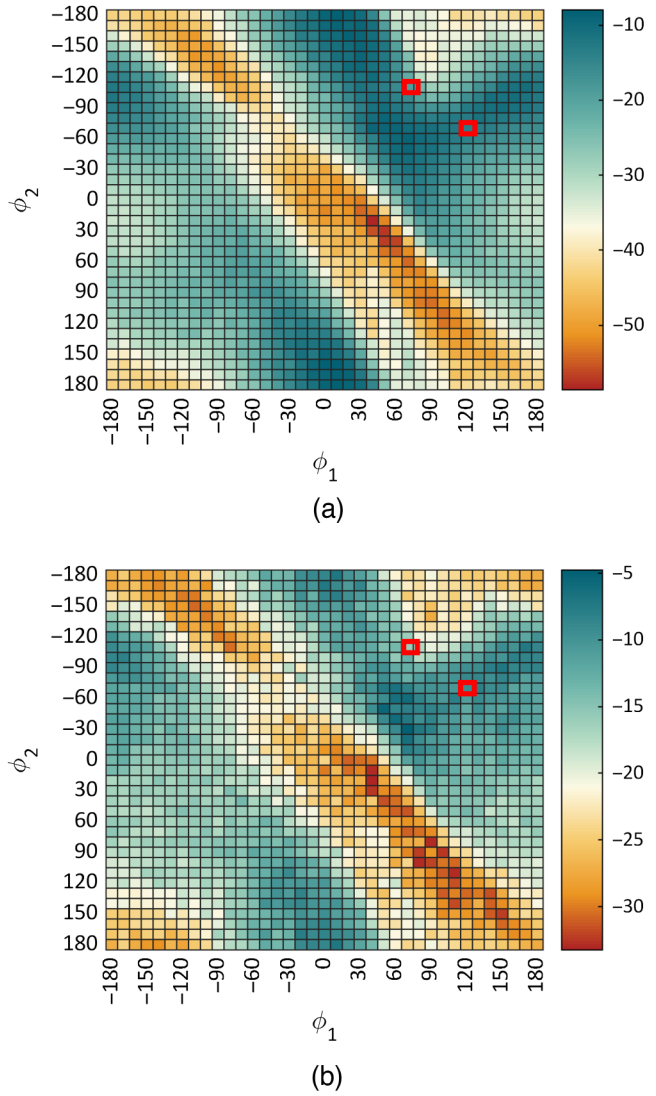

FIG. 21. Error (in %) of measured charge by large 12.5 Ω (a) and compact 50 Ω (b) FCs over 2D rf phase scan. Values above correspond to the charge intercepted by the front face of the FCs, estimated through particle tracking simulations with ASTRA. Notice that the 50 Ω case corresponds to the sum of six narrow-range measurements, as indicated in Table VIII. $\Phi = (120, -70)$ and $\Phi = (70, -110)$ marked in red.

over as many points as desired. An optimum location for the fibers is found in $x = -150$ mm and $z = 3520$ mm (320 mm downstream from the center of the spectrometer) where Fig. 22 shows accurate reconstructions of the main rf working points of interest. However, these calculations are based solely on the absolute number of particles arriving at the fiber location. Further studies, presumably including an experimental calibration, must determine the scintillator response, which depends on the energy and type of incident particles [40]. In addition, background radiation is potentially a major impediment to this measurement, particularly regarding the large amount of γ produced at the target and dark current. The signal readout of the scintillator fiber

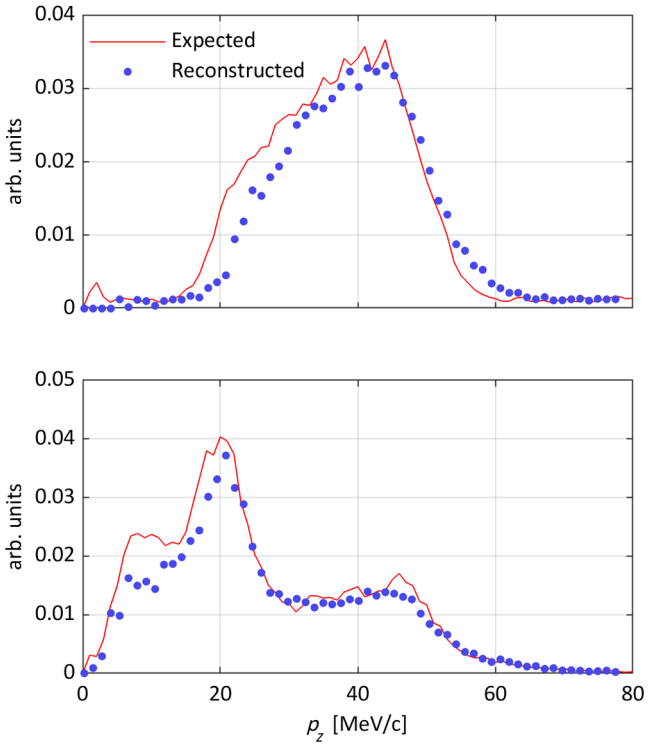

FIG. 22. Estimation of p_z reconstruction for $\Phi = (120, -70)$ (top) and $\Phi = (70, -110)$ (bottom). Computed through 61 ASTRA simulations ranging dipole field strengths from 0 to 0.3 T and scintillator fibers located at $x = -150$ mm and $z = 3520$ mm.

results from the time integration of a photomultiplier waveform generated by the scintillator photoelectron pulse, and thus the time windowing of the waveform integration can suitably restricted to the time duration of the e^+e^- in order to minimize background contribution.

V. EXPERIMENT INSTALLATION

The SwissFEL facility is an ideal host for the P^3 experiment since it can provide a 6 GeV electron beam, corresponding to the nominal drive beam energy of the FCC-ee positron source (see Table II). Two beam lines (Aramis and Athos) are currently operating at SwissFEL, while the accelerator tunnel already foresees space for a future, third beam line (Porthos) leaving enough room for the installation of the P^3 bunker and switchyard.

A. Porthos switchyard

The Porthos switchyard "Phase Planned" is currently being installed following the layout depicted in Fig. 23, which is a simplified version of the final Porthos switchyard "Phase Future," whose design has been reported in [41]. The coordination of the installation is particularly challenging as it can only take place during the regular biannual machine shutdowns, in accordance with the nature of SwissFEL as a user facility.

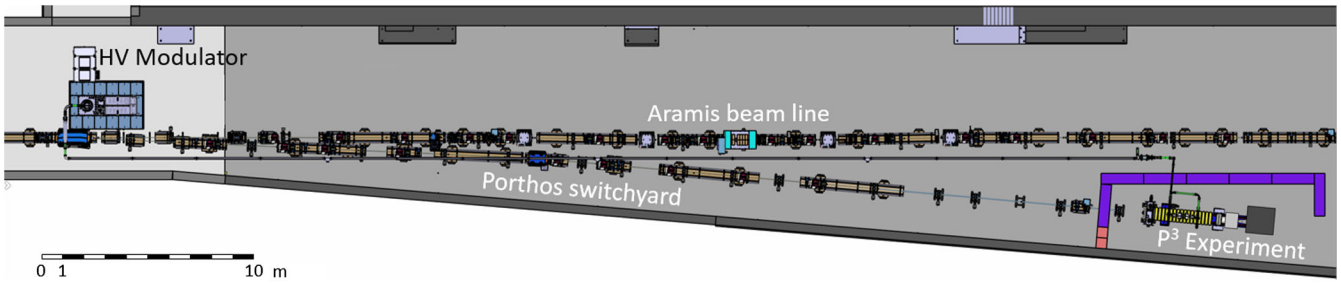

FIG. 23. Top view of the simplified Porthos switchyard (phase planned) and of the P^3 experiment in the SwissFEL facility. In this picture, only the existing Aramis beam line is displayed to appreciate the alternation of short girders in the first part of the new Porthos switchyard. The HV modulator (visible on the left) will be installed in the technical gallery one floor above the accelerator tunnel.

A first static dipole (blue) allows extracting the beam from the Aramis to the Porthos line, meaning that the beam will be available either in the hard x-rays Aramis beam line or in the Porthos switchyard for the P^3 experiment, while a parallel operation of the soft x-rays Athos beam line and of the P^3 experiment is not excluded. Along the Porthos switchyard, we further find nine quadrupoles, six x/y correctors, six beam position monitors (BPMs), two beam loss monitors (BLMs), and one screen to image the beam just before entering the experimental bunker.

B. High-voltage modulator

A new high-voltage (HV) modulator (left in Fig. 23) will be installed in the last available location in the technical gallery, one floor above the accelerator tunnel at a longitudinal coordinate of $z \sim 432$ m ($z = 0$ being the emission plane of the SwissFEL photocathode gun). With the converter target of P^3 at $z \sim 483$ m, a waveguide line of 66 m has been projected to bring rf power in the order of 30 MW to the S-band SW structures of the experiment.

C. P^3 bunker and radiation protection

A bunker consisting of side walls (but no roof) of standard concrete blocks is necessary to shield from the radiation generated during the experiment, when the 200 pC, 6 GeV electron drive beam will impinge on the tungsten target at 1 Hz. The shielding has a double purpose: the respect of the legal dose limits inside and outside the facility, as well as the protection of potentially sensible machine components.

The radiation dose inside and outside the P^3 bunker is calculated through the general purpose Monte Carlo code FLUKA [42] based on a 3D model of the experiment built with Flair interface [43]. Biasing techniques are used to improve the statistics behind the bunker walls. A conservative approach was adopted to design the shielding, as the total dose is calculated by the sum of two separate simulations. First, the interaction of the primary e^- beam from SwissFEL and the W target is simulated according to the parameters in Table II. In this case, the rf accelerating field and the magnetic field of the spectrometer are turned off, resulting in the distribution of Fig. 24. However, a significant part of the secondary e^+ and e^- will be captured by the solenoid channel and are lost in the dump. In a second simulation chain, the e^+e^- distribution is tracked with ASTRA up to the exit of the second rf structure and then imported into FLUKA, where the deflection of the spectrometer and following interaction with the diagnostic section are computed. The dose distributions resulting from the two simulation setups are finally summed up to judge the radiation level at the relevant locations and eventually optimize the shielding.

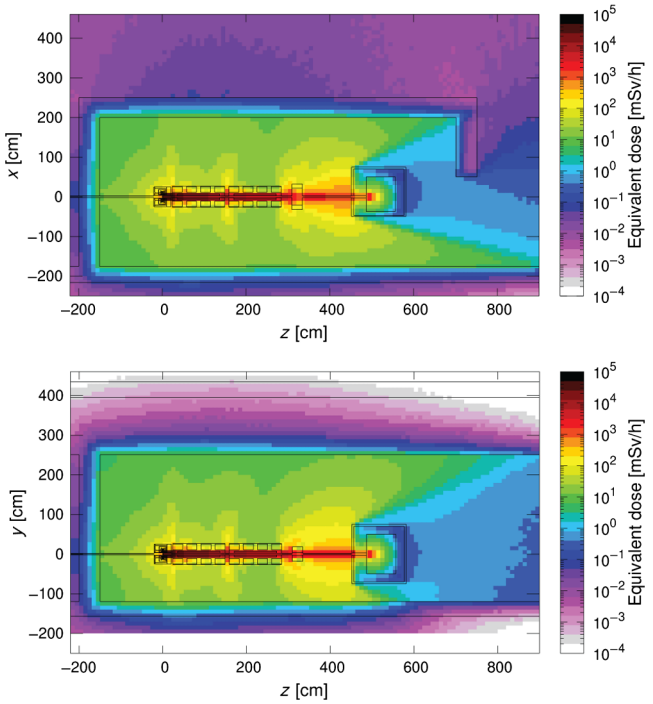

FIG. 24. Ambient dose equivalent in the z–x plane (top) and z–y plane (bottom). No filter on the particle type is applied. No Faraday cup included in the model. Final simulations with all the components in progress.

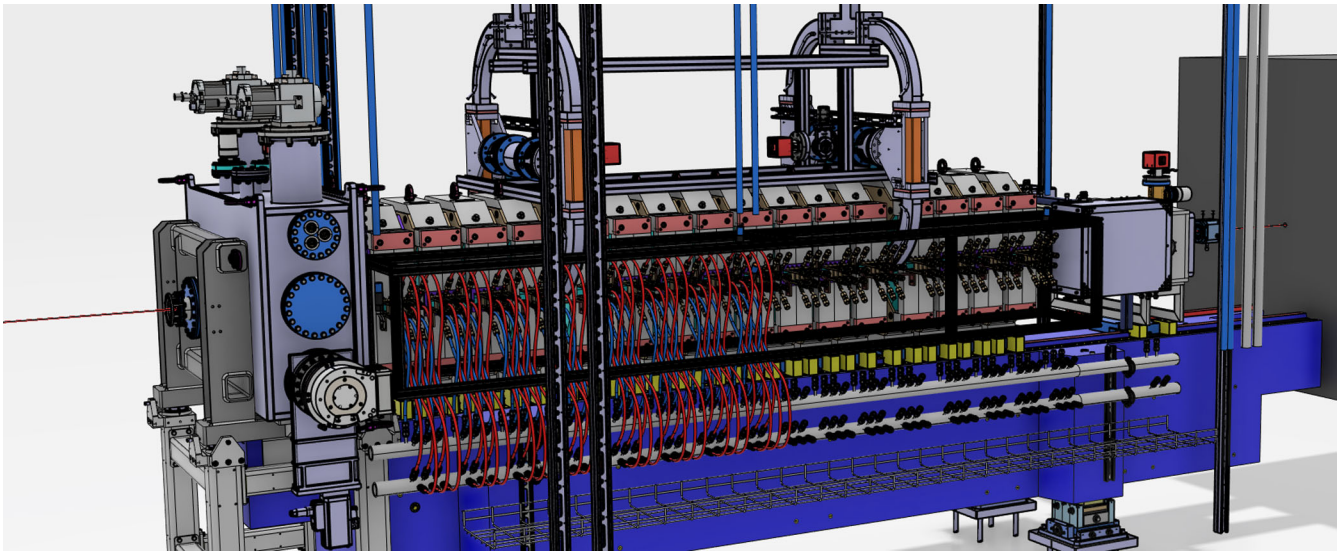

FIG. 25. Reconstruction of P^3 components mounted on a girder, recreated according to latest mechanical design assembly.

VI. CONCLUSION

This paper provided an overview of the P^3 experiment, a proof-of-principle e^+ source particularly well suited for future colliders, due to its potential to enhance e^+ capture and overcome the extreme transverse emittance and energy spread inherent to electron-driven e^+ production. The P^3 project is introduced at a highly developed stage (see Fig. 25), and its design is aimed at increasing the e^+ yield, for which we argue three key factors: high drive linac energy, large transverse aperture, and high solenoid fields around the target and along capture linac. e^+ production will provided by a 6 GeV e^- beam impinging upon a 17.5 mm-thick amorphous tungsten (W) target. The capture section will consist of an HTS solenoid around the target and 2 large aperture rf cavities surrounded by an arrangement of 16 normal conducting solenoids. A pioneer demonstration of HTS non-insulated coil operation at 18 T on axis is also presented.

In addition, physics and beam dynamics associated with the e^+ source and capture system were examined through GEANT4 [22] and ASTRA [23] simulations. The text covered e^+ production at the target and confinement through a 12.7 T peak field enabled by the HTS coils, arguably the main reason behind the enhancement of capture efficiency. Moreover, a comprehensive rf phase optimization was performed based on two figures of merit: captured e^+ charge and its equivalent e^+ yield achieved at the FCC-ee DR. Two rf phase configurations corresponding to the maxima of the above mentioned figures of merit were selected as working points of interest, which are summarized in Table IX. These values conclude an increase of an order of magnitude of the e^+ yield normalized by to primary e^- energy with respect to our predecessors SLC and SuperKEKB.

TABLE IX. Summary of the key e^+ yields envisaged for P^3 at rf working points of interest.

		e^+ charge	Yield normalized to 200 pC
$\Phi=(120,-70)$	Captured	1246 pC	6.23
	Measured by FCs	1129 pC	5.64
	At FCC-ee DR	-	3.84
$\Phi=(70,-110)$	Captured	1153 pC	5.76
	Measured by FCs	971 pC	4.86
	At FCC-ee DR	-	4.64

A concept design of the experiment diagnostics was also presented, as a fundamental part of the experiment that will demonstrate such a yield upgrade. The diagnostics setup consists of an arrangement of broadband pickups, two types Faraday cups, and a variety of scintillating detectors, foreseeing fairly accurate measurements of bunch-by-bunch time structure, charge, and energy spectrum of secondary e^+ and e^- distributions despite their extreme transverse emittance and energy spread. The Faraday cups were studied in greater detail as they will provide the most reliable detection of e^+ charge. According to a preliminary error study based on simulations, we expect successful yield demonstrations over most rf configurations particularly around rf working points of interest (see Table IX). Finally, this paper provided an update on ongoing installation works at SwissFEL, with particular emphasis on the radiation protection bunker, the waveguide network, and the new transfer line *Porthos* branching off from the main SwissFEL linac. The current schedule foresees a first operation with e^+ in 2026.

ACKNOWLEDGMENTS

The authors would like to thank the great support from our colleagues in the rf section at PSI, and all the technical

groups involved in the installation of the P^3 experiment. In addition, we would like to acknowledge the FCC collaboration, and particularly our colleagues at CERN, IJCLab, and INFN involved in the FCC-ee Injector design study. This work was done under the auspices of CHART (Swiss Accelerator Research and Technology).

[1] R. Chehab, Positron sources, in *Proceedings of CERN Accelerator School: 5th General Accelerator Physics Course, Jyvaskyla, Finland* (CERN, Geneva, 1994), pp. 2617–2620, 10.5170/CERN-1994-001.

[2] J. E. Clendenin, High-yield positron systems for linear colliders, in *Proceedings of the 1989 Particle Accelerator Conference, Chicago, IL* (IEEE, New York, 1989), pp. 1107–1112.

[3] I. Chaikovska, R. Chehab, V. Kubytskyi, S. Ogur, A. Ushakov, A. Variola, P. Sievers, P. Musumeci, L. Bandiera, Y. Enomoto, Mark J. Hogan, and P. Martyshkin, Positron sources: From conventional to advanced accelerator concepts-based colliders, J. Instrum. **17**, P05015 (2022).

[4] SLAC Linear Collider Design Handbook, Report No. SLAC-R-714, 1984.

[5] K. Akai, K. Furukawa, and H. Koiso, SuperKEKB Collider, Nucl. Instrum. Methods Phys. Res., Sect. A **907**, 188 (2018).

[6] E. Prat *et al.*, A compact and cost-effective hard X-ray free-electron laser driven by a high-brightness and low-energy electron beam, Nat. Photonics **14**, 748 (2020).

[7] T. Suwada, M. A. Rehman, and F. Miyahara, First simultaneous detection of electron and positron bunches at the positron capture section of the SuperKEKB factory, Sci. Rep. **11**, 12751 (2021).

[8] Y. Enomoto *et al.*, Development of a flux concentrator for SuperKEKB, in *Proceedings of the 13th annual meeting of Particle Accelerator Society of Japan, Chiba, Japan* (Particle Accelerator Society of Japan, Tokyo, 2016), p. 1420.

[9] P. Craievich *et al.*, FCC-ee injector study and the P^3 project at PSI, CHART Scientific Report (2022), https://www.chart.ch.

[10] Future Circular Collider study, https://fcc.web.cern.ch/.

[11] M. Benedikt, F. Zimmermann *et al.*, FCC-ee: The lepton collider. Future circular collider conceptual design report volume 2, Eur. Phys. J. Spec. Top. **228**, 261 (2019).

[12] P. Craievich *et al.*, The FCCee pre-injector complex, in *Proceedings of 13th International Particle Accelerator Conference, IPAC-2022, Bangkok, Thailand* (JACoW, Geneva, Switzerland, 2022), pp. 2007–2010, 10.18429/JACoW-IPAC2022-WEPOPT063.

[13] P. Craievich, M. Schaer, N. Vallis, and R. Zennaro, FCC-ee injector study and the P^3 project at PSI, CHART Scientific Report (2021), https://www.chart.ch.

[14] I. Chaikovska *et al.*, Positron source for FCC-ee, *in Proceedings of the IPAC'19, Melbourne, Australia* (JACoW, Geneva, Switzerland, 2019), pp. 424–427, 10.18429/JACoW-IPAC2019-MOPMP003.

[15] Y. Zhao *et al.*, Comparison of different matching device field profiles for the FCC-ee positron source, in *Proceedings of the 10th International Particle Accelerator Conference, IPAC'21, Campinas, SP, Brazil* (JACoW, Geneva, Switzerland, 2021), pp. 2617–2620, 10.18429/JACoW-IPAC2021-WEPAB015.

[16] Y. Zhao, B. Auchmann, I. Chaikovska, R. Chehab, P. Craievich, S. Döbert, D. Duda, J. Kosse, A. Latina, P. Martyshkin, S. Ogur, and R. Zennaro, Optimisation of the FCC-ee positron source using a HTS solenoid matching device, in *Proceedings of 13th International Particle Accelerator Conference, Bangkok, Thailand* (JACoW, Geneva, Switzerland, 2022), pp. 2003–2006, 10.18429/JACoW-IPAC2022-WEPOPT062.

[17] B. Humann *et al.*, Radiation load studies for the FCC-ee positron source with a superconducting matching device, in *Proceedings of 13th International Particle Accelerator Conference, IPAC'22, Bangkok, Thailand* (JACoW, Geneva, Switzerland, 2022), pp. 2879–2882, 10.18429/JACoW-IPAC2022-THPOTK048.

[18] S. Hahn, D. K. Park, J. Bascunan, and Y. Iwasa, HTS pancake coils without turn-to-turn insulation, IEEE Trans. Appl. Supercond. **21**, 1592 (2011).

[19] D. Hahn, K. Kim, H. Lee, and Y. Iwasa, Current status of and challenges for no-insulation HTS winding technique, Teion kogaku **53**, 2 (2018).

[20] D. X. Fischer, R. Prokopec, J. Emhofer, and M. Eisterer, The effect of fast neutron irradiation on the superconducting properties of REBCO coated conductors with and without artificial pinning centers, Supercond. Sci. Technol., **31**, 044006 (2018).

[21] Sumitomo RDK500B, https://www.shicryogenics.com.

[22] GEANT4: Toolkit for the simulation of the passage of particles through matter, https://geant4.web.cern.ch/.

[23] ASTRA: A space charge tracking algorithm, https://www.desy.de/~mpyflo/.

[24] Y. Zhao, A. Latina, S. Doebert, D. Schulte, and L. Ma, Optimisation of the CLIC positron source at the 1.5 TeV and 3 TeV stages, Reports No. CERN-ACC-2020-0026 and CLIC-Note-1165.

[25] K. Floettmann, Some basic features of the beam emittance, Phys. Rev. ST Accel. Beams **6**, 034202 (2003).

[26] R. H. Helm, Adiabatic approximation for dynamics of a particle in the field of a tapered solenoid, SLAC Report No. 4, 1962.

[27] R. Chehab, Positron sources, in *Proceedings of CERN Accelerator School: 3rd General Accelerator Physics Course, Salamanca, Spain* (CERN, Geneva, 1988), pp. 105–132, 10.5170/CERN-1989-005.

[28] E. Bulyak, V. Mytrochenko *et al.*, Theoretical investigations on the adiabatic matching device–based positron capture system, arXiv:2207.06126.

[29] N. Vallis *et al.*, The PSI positron production project, in *Proceedings of LINAC'22, Liverpool, UK* (JACoW, Geneva, Switzerland, 2023), pp. 577–580. 10.18429/JACoW-LINAC2022-TUPORI16.

[30] B. Aune and R. H. Miller, New method for positron production at SLAC, Report No. SLAC-PUB-2393, 1979.

[31] CST Studio Suite Electromagnetic Simulation Solvers, https://www.3ds.com.

[32] 27 GHz SMA Feedthrough for UHV Applications 242-SMAD27G-C16, Allectra GmbH (2019).

[33] Microwave 1.85 mm (SMA) feedthrough 242-SMAD65G-C16, Allectra GmbH (2022).

[34] 1.85 mm male to 3.5 mm male cable assemblies, Pasternack Enterprises, https://www.pasternack.com/1.85mm-male-to-3.5mm-male-cable-assemblies-category.aspx.

[35] T. Suwada, M. A. Rehman, and F. Miyahara, First simultaneous detection of electron and positron bunches at the positron capture section of the SuperKEKB factory, Sci. Rep. **11**, 12751 (2021).

[36] T. Suwada, Direct observation of positron capture process at the positron source of the SuperKEKB B-factory, Sci. Rep. **12**, 18554 (2022).

[37] A. Angelovski, A. Kuhl, M. Hansli, A. Penirschke, S. M. Schnepp, M. Bousonville, H. Schlarb, M. K. Bock, T. Weiland, and R. Jakoby, High bandwidth pickup design for bunch arrival-time monitors for free-electron laser, Phys. Rev. ST Accel. Beams **15**, 112803 (2012).

[38] Ansys HFSS, Best-in-class 3D high frequency structure simulation software, https://www.ansys.com.

[39] C. D. Johnson, The development and use of alumina ceramic fluorescent screens, CERN Report No. CERN-PS-90-42-AR, 1990.

[40] J. B. Birks, Absorption of incident radiation, in *The Theory and Practice of Scintillation Counting* (Pergamon Press, Oxford, UK, 1964), pp. 15–38.

[41] S. Reiche *et al.*, Design considerations for the extraction line of the Proposed Third Beamline Porthos at SwissFEL, in *Proceedings of FEL'22, Trieste, Italy* (JACoW, Geneva, Switzerland, 2022), https://indico.jacow.org/event/44/contributions/532/.

[42] The Official FLUKA Site, http://www.fluka.org/.

[43] V. Vlachoudis, FLAIR: A powerful but user friendly graphical interface for FLUKA, in *Proceedings of International Conference on Mathematics, Computational Methods & Reactor Physics, Saratoga Springs, New York* (American Nuclear Society in Downers Grove, Illinois, USA, 2009), pp. 790–800.